Photocatalytic properties of atomic layer deposited TiO2 inverse opals and planar films for the degradation of dyes

Pierre Birnal, M.C. Marco de Lucas, I. Pochard, B. Domenichini, L. Imhoff

Photocatalytic properties of atomic layer deposited TiO_2 inverse opals and planar films for the degradation of dyes

P. Birnal [a], M. C. Marco de Lucas [a,*], I. Pochard [b], B. Domenichini [a], L. Imhoff [a]

[a] *Laboratoire Interdisciplinaire Carnot de Bourgogne (ICB), UMR 6303 CNRS-Université Bourgogne-Franche Comté, 9 Av. A. Savary, BP 47 870, F-21078 DIJON Cedex, FRANCE*

[b] *Laboratoire UTINAM, UMR 6213 CNRS-Université Bourgogne-Franche-Comté, Besançon, France*

Abstract

The pollution of waste water due to organic dyes used in textile and chemical industries is an important environmental issue. Inverse opals (IO) offer a great potential for increasing the efficiency of semiconductor photocatalysts as TiO_2 by the synergy of high specific surface and photonic crystal properties.

In this work, we report the synthesis of both IO and planar TiO_2 films by Atomic Layer Deposition and a comparative study of their photocatalytic activity for the degradation of methylene blue in water under UV irradiation. The porosity of planar TiO_2 films was modified by a pre-treatment of the substrate to analyze its effect on the photocatalytic activity. A rutile single-crystal was also used for comparison. The kinetics of the MB degradation process was studied for long times to investigate the eventual effect of the progressive increase of degradation products in the solution.

A degradation percentage about 90% was obtained after 10 hours using IO films, and only about 60% by using planar and dense films. A first-order reaction kinetics was shown in the case of IO films. For the other catalysts, a slowing-down of the reaction kinetics was shown above 8 h. The adsorption of the degradation products at the catalyst surface was addressed to explain this effect. The results highlight the potential of IO films synthesized by ALD for photocatalytic applications.

Key words: inverse opals, photocatalysis, dyes degradation, ALD

* Corresponding author
Email address: delucas@u-bourgogne.fr (M. C. Marco de Lucas).

1 Introduction

Titanium dioxide is widely used as a photocatalyst because of its oxidizing properties, its reasonable cost, good chemical stability and poor toxicity [1–3]. It is used in different fields of application linked to energy storage and environment [4–6]. In this latter field, the pollution due to organic dyes used in textile and chemical industries is an important environmental issue. It has been estimated that around 15% of the total world production of dyes is discharged as waste water [7]. These pollutants are generally considered to be toxic for animals and plants, and most of them are poorly biodegradable or resistant to environmental conditions [8].

Different methods have been used to enhance the photocatalytic activity of titanium dioxide, the main drawbacks being the necessity of UV radiation and the high recombination rate of photo-generated electron-pairs [9]. Many works have also been devoted to increase the specific surface area of photocatalysts in order to take full advantage of their properties. The synthesis of photocatalysts displaying the morphology of inverse opals (IO) fits this approach [10–14], but the interest of IO photonic crystals goes further because of their specific optical properties due to the photonic band gap [15]. In particular, the decrease of the velocity of light propagation at the edge of the photonic band induces reflections in the material that can enhance its optical absorption. The synergy of both the photonic crystal properties and the high specific surface offers a great potential for IO crystals in photocatalysis [16–18].
Inverse opal materials are usually fabricated by using a template formed by an ordered set of silica or polymer micro-spheres. The template is impregnated by the material, and finally is removed by calcination or etching. Sol-gel methods, electrochemical deposition, chemical vapor deposition and atomic layer deposition have been mainly used for this process [18]. In this work, titanium dioxide IO films were synthesized by using Atomic Layer Deposition (ALD) on ordered films of polystyrene (PS beads). The ALD technique allows an excellent control of the synthesized film at the expense of a lower growth rate than the classical Chemical Vapor Deposition (CVD) process [19,20]. Moreover, ALD is used to fabricate films with a very good conformity on complex shape substrates because the gas flow bringing the precursors will cover every available surface. The result is a homogeneous layer on the substrate with a perfectly controlled thickness. This technique is mainly used for the synthesis of oxides, carbides or metals [21–24]. Compared to the CVD process, the ALD technique can operate at lower temperature, which allows the use of substrates with a low degradation temperature, as polymers.

The aim of this work was to investigate the photocatalytic activity of titanium dioxide IO films synthesized by ALD for the degradation of dyes, and compare this activity to that of planar titanium dioxide films synthesized on silicon substrates by using the same ALD experimental conditions. Moreover, a pre-treatment of the Si substrates was also used to modify the growth of the titanium dioxide film in order

to promote the growth of porous films. The goal was to show the effects due to the high specific surface which is inherent of the IO morphology.
Structural and chemical analysis of the synthesized IO films were done by Raman spectroscopy and XPS, and compared to films obtained on silicon substrates. The photocatalytic tests were focused on the degradation of methylene blue (MB), which is widely used in textile industry as a blue dye. Previous studies about photodegradation of dyes using TiO_2 as a catalyst have reported a phenomenon of limitation of the degradation process due to the formation of intermediate products that can hinder the interactions at the interface between the reactants and the photocatalyst [25]. It will be shown here that this effect can be reduced by using IO films.

2 Experimental details

2.1 ALD process

All the samples were elaborated on silicon (100) substrates cleaned by successive solvent baths (cyclohexane, acetone and ethanol) using a Direct Liquid Injection Metal-Organic Chemical Vapor Deposition (DLI-MOCVD) process with rapid thermal heating. The Direct Liquid Injection (DLI) system (Annealsys MC-050) is based on the atomized liquid injection of the precursor solution to generate the reactive vapor. According to the operating parameters, this device works in CVD or ALD mode [26,27].
The silicon substrates were laid on a silicon carbide coated graphite susceptor supported by a quartz holder inside a quartz reactor. The reaction chamber was kept under a working pressure below 20 mbar using a dry pump and a regulator valve. The temperature of the susceptor near the sample was measured by a K-type thermocouple and maintained at 90 °C during the deposition process.

2.2 Synthesis of dense and porous TiO_2 films

The precursors used to synthesize TiO_2 films by ALD were Tetrakis (dimethylamido) titanium(IV) (TDMAT, Sigma Aldrich, 99.999%) and deionized water. The titanium precursor solution was a 0.02 M solution of TDMAT in anhydrous cyclohexane (C_6H_{12}, 99.99%, Sigma Aldrich) which meets the requirements for the DLI-CVD process: no interaction of the solvent with the TDMAT precursor, high vapor pressure, good thermal stability, low viscosity, low cost and no toxic. TDMAT was chosen as a titanium precursor because it allows working at a lower temperature compared to others titanium precursors such as $TiCl_4$ that need an important energy to break the Ti-Cl bond to synthesize TiO_2 [28]. Furthermore,

Working pressure	20 mbar
Substrate temperature	90 °C
N_2 carrier gas flow	100 sccm
TDMAT injection opening time	30 ms
Purges duration	7 s
Water injection opening time	75 ms

Table 1
Experimental conditions used in this work for the synthesis of dense TiO_2 films by Atomic Layer Deposition.

TDMAT does not release corrosive products like HCl in the case of titanium tetrachloride [29,30]. In comparison with another metal-organic precursor such as titanium isopropoxide (TTIP), TDMAT induces less carbon pollution in the deposited TiO_2 films. The TDMAT precursor vessel was kept at room temperature and pressurized under 3 bars of 99.999% pure nitrogen (N_2) used as carrier gas. Deionized water, H_2O, was used as the second precursor. It was kept in a tank under vacuum to obtain a saturated vapour atmosphere to be injected into the reaction chamber. The precursors were introduced by Direct Liquid Injection as micro-droplets in the vaporization chamber at 150 °C. After the flash evaporation of the precursor, the vapour was carried into the reaction chamber by the nitrogen carrier gas. TiO_2 deposition by Atomic Layer Deposition was made by a repetition of multiple cycles comprising four steps: injection of TDMAT, a first purge, injection of deionized water and a second purge. All the deposition conditions are summarized in Table 1. The thickness of the deposited TiO_2 film was measured by profilometry using a silicon substrate with a masked area during the deposition process.

Porous TiO_2 films were fabricated by a pre-treatment of the silicon surface. The pre-treatment was an injection of liquid H_2O in the reaction chamber during several minutes with a frequency of 1 Hz and a 5 ms injector opening time. Water in the tank was kept at 1 bar. Just after the pre-treatment of the substrate, the TiO_2 film was synthesized by using the same experimental conditions previously described to obtain dense TiO_2 films.

2.3 Synthesis of TiO_2 inverse opals

Inverse opals of titanium dioxide were fabricated by three successive steps: the first step was the deposition of 500 nm diameter polystyrene (PS) beads (from Alfa Aesar) on a silicone substrate, the second one was the deposition of a dense TiO_2 film by ALD and the final step was the annealing of the sample in order to burn the PS beads and to induce the crystallization of TiO_2 in the anatase phase.
The PS beads were deposited at room temperature by spin coating using a 2.5 wt%

suspension of PS beads in water. The spin coating process was done with an acceleration of 100 tr/min/s, a programmed steady speed of 1500 tr/min, and a total duration of 60 s. Within these conditions, monolayers or bilayers of PS beads were mainly obtained. After deposition of the TiO_2 film, the samples were annealed at 380 °C during three hours in the reaction chamber of the DLI-CVD system under a pressure of 10 mbar.

2.4 Characterization methods and photocatalysis experiments

Raman spectroscopy was used to investigate the structural properties of the films. Spectra were made at room temperature using a Renishaw inVia micro-Raman spectrometer in backscattering configuration. The spectra were recorded with a 532 nm wavelength laser as excitation source, the laser power was about 0.5 mW to avoid heating the samples.
The surface and cross-section morphology of the samples were observed by scanning electron microscopy (SEM) by using a JEOL 7600F working between 1 and 3 kV. A surface ion-polishing of the inverse opals samples was used to crush the TiO_2 shells in order to investigate their inner side. The ion-polishing process was done during 15 min by using an Ar^+ beam with an energy of 4 keV.
Characterizations of the chemical composition of TiO_2 films were performed by X-ray photoelectron spectroscopy (XPS) using an Al Kα X-ray source at 1486.6 eV. Electron detection was provided by a hemispheric analyzer CLAM 4 MCD (Thermo VG Scientific). Photoelectrons were collected with an analyzer slit of 2 mm and a pass energy of 100 eV for survey spectra and of 20 eV for the spectral ranges corresponding to Ti2p and O1s lines.
The photocatalytic properties of the different samples were studied by measuring the degradation of a methylene blue (MB) solution concentrated at 1 μmol/L. The MB solution was placed in a cuvette (1x1x3 cm^3) together with a sample of the catalyst (1 cm^2), and the system was shaken during 10 minutes by ultrasounds. UV irradiation of the catalyst was done by using an UV lamp at 365 nm. The evolution over the time of the solution absorbance was measured with a Shimadzu UV-2550 spectrometer at regular intervals. Three types of films were studied in this way: dense and porous films, and IO films. Moreover, the same degradation experiments were done with bulk TiO_2 as catalyst by using a (110) rutile single-crystal with a surface of 1 cm^2.

3 Results and discussion

3.1 Morphological characterizations

The morphology of the deposited films was observed by SEM in the secondary electron mode. Figures 1a and 1b show the images obtained for a dense TiO_2 film obtained by 1500 ALD cycles. The image of the surface (Fig.1a) shows a very homogeneous deposit with a grain size about 8 nm. The cross-section view (Fig.1b) shows that the film is dense and homogeneous in-depth. The thickness of the film is 216 $\pm$3 nm, which corresponds to a growth rate of 0.14 nm/cycle.

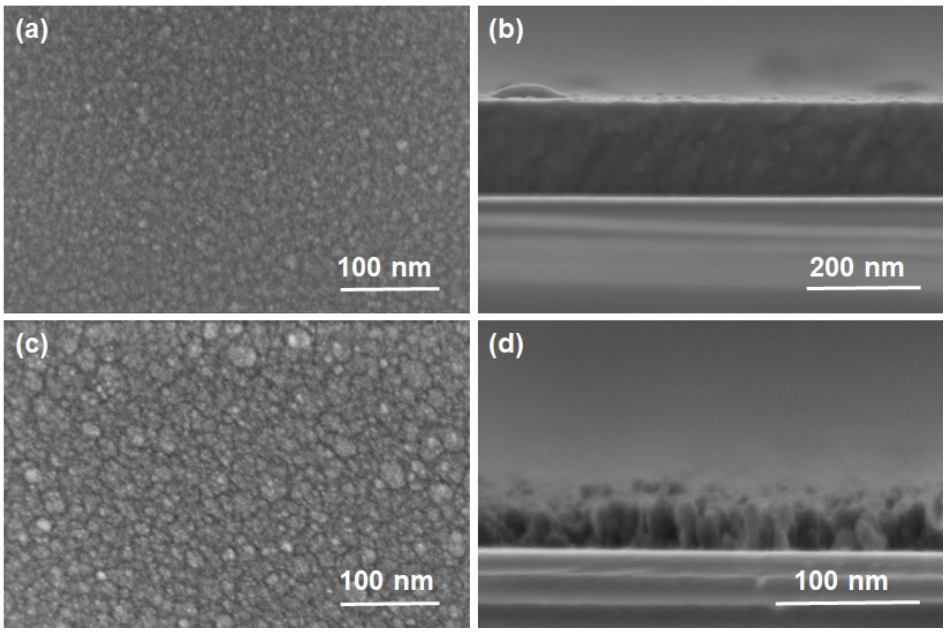

Fig. 1. FE-SEM surface (a,c) and cross-section (b,d) images of TiO_2 films deposited on Si substrates. (a,b) Dense TiO_2 film (1500 ALD cycles), and (c,d) porous film (250 ALD cycles). Images were taken in secondary electrons mode.

The second kind of ALD films studied by SEM was porous TiO_2 films. Figure 1c shows a rougher surface compared to Fig.1a, and grains about 10-20 nm in size. The cross-section image (Fig.1d) shows a less compact film compared to the dense film given in Fig.1b. The thickness of the film is around 37 nm. These results show that the injection of liquid water on the silicon substrate preceding the TiO_2 fabrication modifies the first stages of the growth of the film, which induces the formation of a porous layer. However, the growth rate of the film is nearly the same as for the growth of dense TiO_2 films.

Figure 2a displays the arrangement of PS beads on the silicon substrate before the deposition of a TiO_2 film. It can be seen that the beads are orderly organized corresponding to a (111) plan of a centered-face cubic structure. IO films were obtained

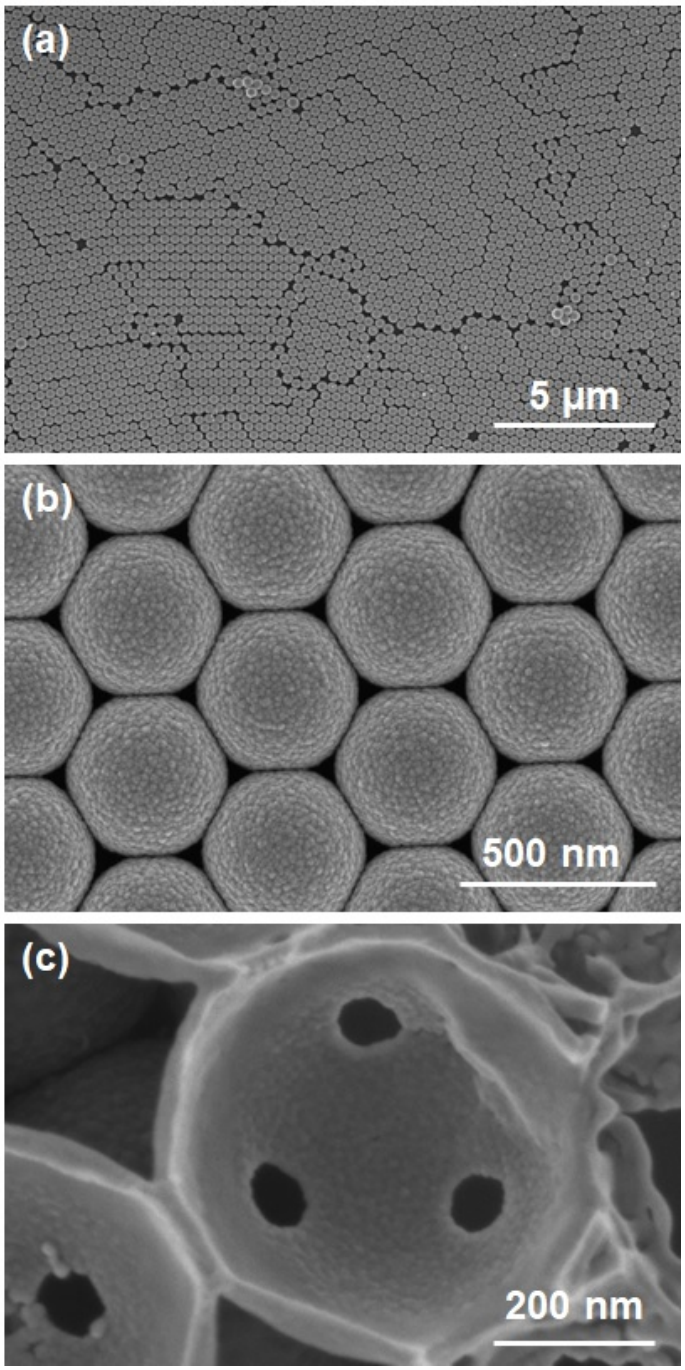

Fig. 2. FE-SEM surface images of TiO_2 inverse opals (250 ALD cycles). (a) As-deposited sample, (b) after annealing at 380 °C, and (c) after ion-polishing of the annealed sample. FE-SEM images were taken in secondary electron mode.

by the synthesis of a 35 nm TiO_2 layer on the PS beads, followed by annealing during 3 hours at 380 °C. Figure 2b displays a surface view after the annealing process. It shows that a homogeneous film has perfectly covered the PS spheres, as it was expected by using an ALD process (Fig. S1 and S2). The small deformation of the spheres can be explained by the softening of PS during the ALD process at 90 °C.

The free space between the spheres is reduced and an incipient sintering between them can be observed.
An ion-polishing treatment of the deposits allowed to remove the upper part of the spheres (Fig. 2c, and Fig. S3). It can be observed that the polystyrene beads have been totally burned out giving rise to a network of TiO_2 interconnected spherical shells about 35 nm thick. This shows that the ALD process allowed covering with a homogeneous TiO_2 film not only the top of the PS beads, but their whole surface. Only the points of contact between neighboring PS beads were not covered with TiO_2, which explains the holes observed in Figure 2c. These holes are channels connecting neighboring shells which can enhance the photocatalytic efficiency thanks to the high surface available for the adsorption of reactive molecules.

3.2 Structural and chemical analysis of the films

Raman spectroscopy was used to investigate the crystalline structure of the different films before and after the annealing treatment at 380 °C (Fig.3). The spectra of as-deposited films showed for all the samples only the peaks corresponding to the silicon substrate. As expected, taking into account that the ALD process was carried out at 90 °C, the analyses showed that the as-deposited TiO_2 films were amorphous. After annealing, the Raman spectra of dense, porous and IO films (Fig.3) showed new peaks at 145, 400 and 640 cm^{-1} that can be assigned to the anatase phase of TiO_2 [31]. The three kinds of samples, dense, porous and IO films, showed the Raman fingerprint of the anatase phase attesting the crystallization of amorphous TiO_2 into the anatase phase.
For the IO film (Fig.3), it is worth to note the high intensity of the anatase peaks compared to those of the silicon substrate. The thickness of the TiO_2 shells is only about 35 nm, but the morphology of the film leads to a total thickness of TiO_2 analysed by Raman which is quite higher.
In the high frequency range of the spectra, two bands at 1380 and 1590 cm^{-1} appear in the spectra of annealed samples. They can be assigned, respectively, to the D and G bands of amorphous carbon [32]. The presence of amorphous carbon was also observed after annealing in dense TiO_2 films deposited on silicon substrates devoid of PS beads. So it cannot be due to residues of the combustion of polystyrene beads. This carbon pollution of the films can come from remaining residues of the precursor molecules. The low temperature used for the ALD process can promote this effect.

X-ray photoelectron spectroscopy (XPS) was used for chemical state analysis on the surface of the films. As-deposited and annealed samples of dense, porous and IO films were used for XPS analysis. Figures 4 and 5 show the spectra of Ti2p and O1s lines obtained for dense films. The results were similar for porous and IO films. Only a minor difference in the O1s line of as-deposited IO films will be analyzed below.

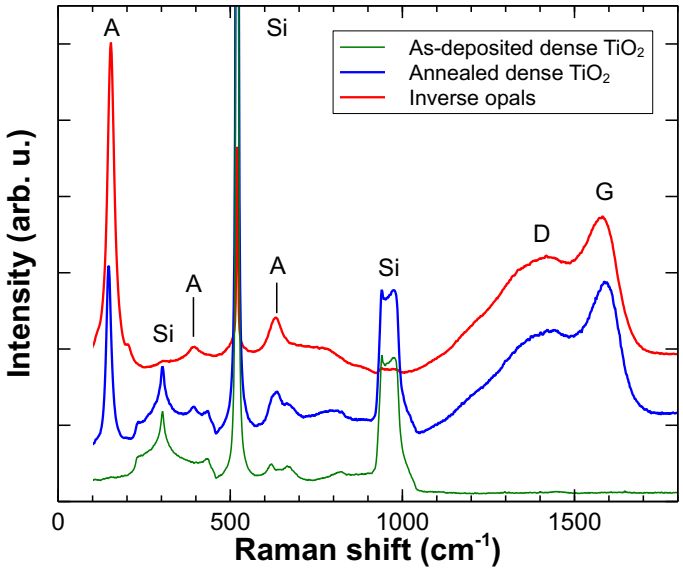

Fig. 3. Raman spectra of a dense TiO_2 layer before and after annealing at 380 °C during 3 hours, and an inverse opals layer after the same annealing.

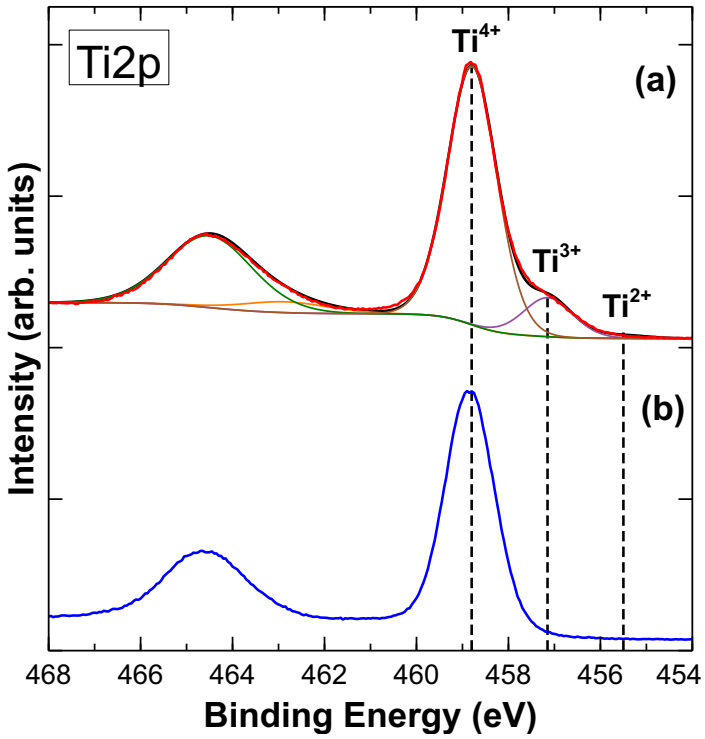

Fig. 4. Ti2p XPS spectra of dense TiO_2 films: (a) as-deposited and (b) annealed samples.

For the annealed films, the spectrum of the Ti2p line (Fig.4) shows only the $Ti2p_{3/2}$ and $Ti2p_{1/2}$ peaks of Ti^{4+} at 458.80 eV and 464.50 eV, respectively. The interval between both peaks is equal to 5.7 eV which attests that at least 99% of titanium is in the Ti^{4+} oxidation state [33]. This demonstrates the obtaining of stoichiometric TiO_2 after the annealing treatment. Before annealing, the spectrum of the Ti2p line

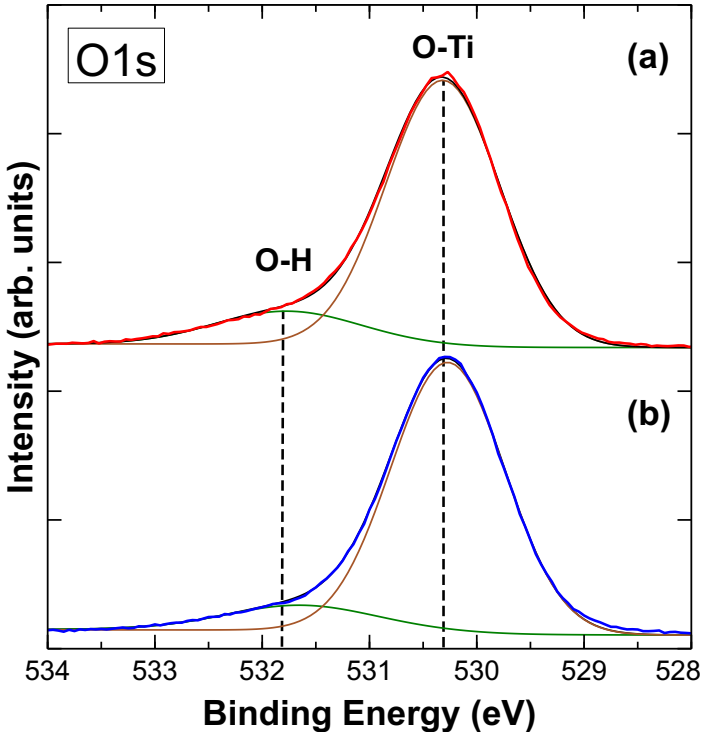

Fig. 5. O1s XPS spectra of dense TiO_2 films: (a) as-deposited and (b) annealed samples.

for as-deposited samples shows, together with the peaks corresponding to Ti^{4+}, the presence of reduced titanium components corresponding to Ti^{3+} and Ti^{2+} [34]. Considering the relative areas of Ti^{4+}, Ti^{3+} and Ti^{2+} components, the stoichiometry can be estimated to be $TiO_{1.93}$.

The spectrum of the O1s line (Fig.5) shows for both as-deposited and annealed films, a main component at 530.20 eV which matches the expected value for stoichiometric TiO_2 [35]. A quite smaller component at 531.80 eV can be assigned to surface adsorbed OH groups [36]. The relative intensity of this component was higher in the case of IO films compared to dense and porous films. This can be explained by the fact that the analysis carried out on IO films involves a larger surface area compared to planar films, which enhances the contribution of species adsorbed on the surface as hydroxyl groups.

The results obtained by Raman spectroscopy and XPS demonstrate that the annealing treatment of the films is not only the final step of the process required here for obtaining inverse opals, but it is also necessary for obtaining stoichiometric TiO_2 crystallized in the anatase phase.

3.3 Photocatalytic tests: degradation of methylene blue

The degradation reaction of methylene blue was used to study the photocatalytic activity of the IO films compared to dense and porous TiO_2 films. For the three kind of films, the thickness of the deposited TiO_2 layer was about 40 nm. All the

test were done by using annealed films. For comparison, the same experiments were done by using a (110) rutile single-crystal. The evolution over the time of the MB solution concentration was measured by UV-Vis optical absorption. The eventual degradation of MB under UV irradiation in the absence of any catalyst was also studied. The results are given in Figure S4. After exposition to UV light during 48 h, the intensity decrease of the MB absorption band was less than 5%, which is more than 10 times smaller than the degradation obtained with all the photocatalysts studied here.

Figure 6a shows the optical absorption spectra of MB solutions after 2 hours of UV irradiation. The natural degradation of MB molecules under UV light exposure in the absence of any catalyst was negligible. The corresponding absorbance spectrum was used as a reference. The effect of regular agitation of the solution was also checked by sonication during 10 min every hour. The results showed a negligible effect.

The absorption spectrum of the MB solution shows (Fig.6a) a main band at about 663 nm, and a lower intensity band at about 604 nm. After UV irradiation during two hours, the absorption bandshape is similar to the reference independently the catalyst used for the degradation of MB molecules, but the absorbance decreases differently as a function of the catalyst. The rutile single-crystal shows a very low effect compared to the films. The porous film allows to obtain a higher effect than the dense films which is in agreement with the higher surface available for the adsorption of MB molecules. The highest degradation is obtained with IO films.

For longer UV irradiation times, the absorption bandshape varies mainly when using IO films as a catalyst. Figure 6b displays the optical absorption spectra of MB solutions after 10 hours of UV irradiation by using IO films. The absorbance at 663 nm decreases faster than at 604 nm. The relative intensity of both bands is nearly the same after 5 hours of irradiation, but after 10 hours the band at 663 nm is very low. Previous works [37] have related the band at 604 nm with dimerization of MB, whereas the main band at 663 nm is assigned to individual MB molecules. The evolution of the spectra given in Figure 6b suggests a faster decrease of the concentration of MB single molecules than of dimers by using IO films as a catalyst. To go further, the kinetics of the degradation process has been studied for the different photocatalysts.

Figure 7a shows the variation over the time of the degradation percentage of MB in the solution defined by eq. 1, for the different catalysts.

$$Degradation\ (\%) = (C_t/C_0) \cdot 100 \tag{1}$$

with C_t the concentration of the MB solution at time t, and C_0 the initial concentration. On the basis of the Beer-Lambert law, the C_t/C_0 ratio was taken equal to the absorbance ratio A_t/A_0, with A_t and A_0 being the absorbance at the 664 nm band

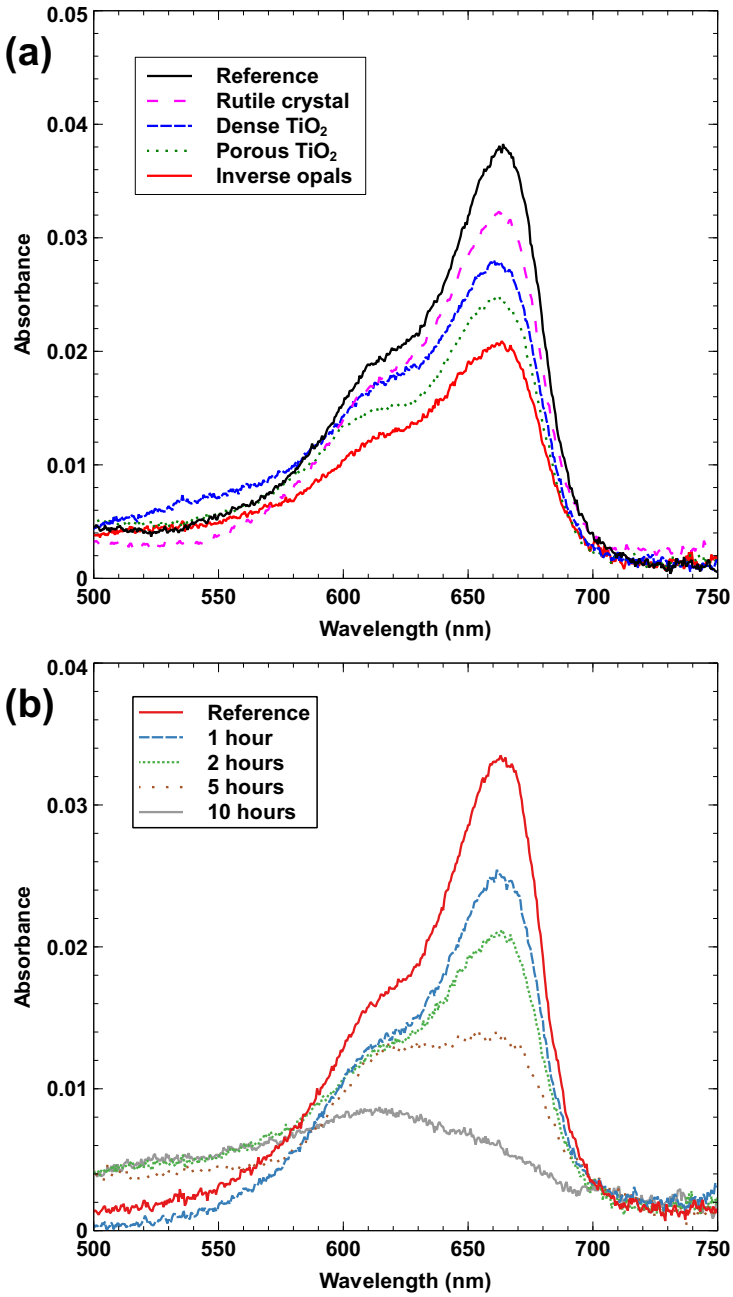

Fig. 6. (a) Optical absorption spectra of a methylene blue solution initially concentrated at 1 μmol/L after 2 hours of UV irradiation of four different catalysts plunged into the MB solution: a rutile single-crystal, a dense TiO_2 film, a porous TiO_2 film and a TiO_2 inverse opal film. The spectrum of the MB solution in the absence of catalyst is taken as the reference. (b) Evolution of the absorbance of the methylene blue solution initially concentrated at 1 μmol/L exposed to UV light in presence of inverse opals during 10 hours. The surface of the catalysts substrate was 1 cm^2.

maximum (after subtracting of the background) at time t and at $t = 0$, respectively.

The degradation of MB is much faster and efficient by using IO film than the other

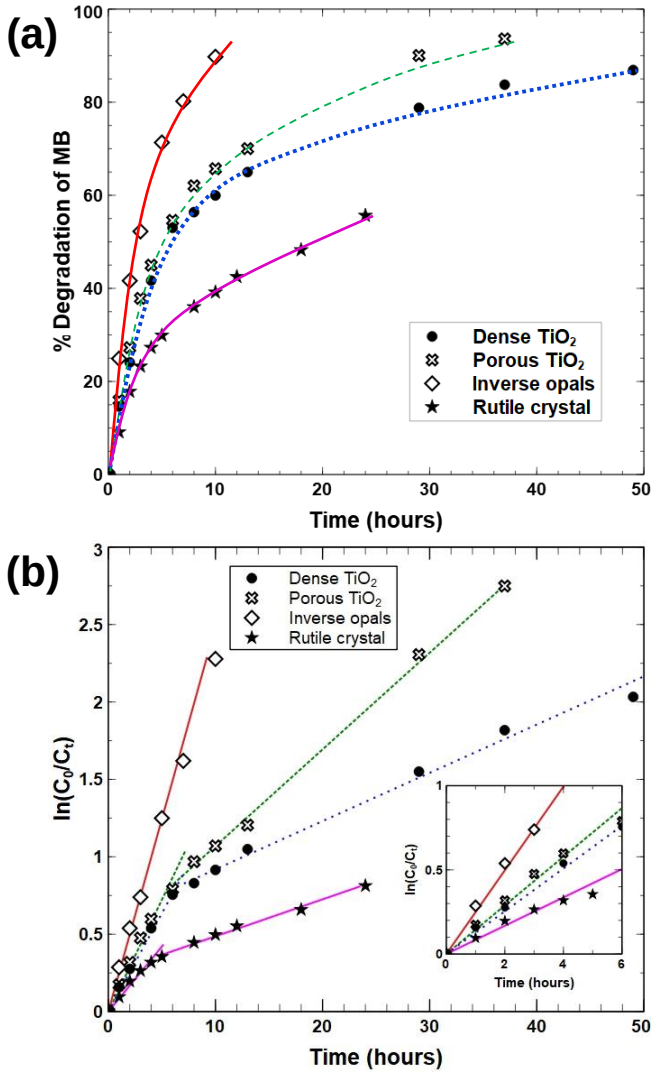

Fig. 7. (a) Over time degradation of a methylene blue solution initially concentrated at 1 μmol/L in presence of four different catalyst (IO film, dense and pourous planar films and a rutile single-crystal). The surface of the catalysts substrate was 1 cm^2. (b) Kinetic curves for the photocatalytic degradation of methylene blue in presence of each catalyst.

catalysts used in this work. After 2 hours of UV irradiation the degradation of MB is about 42 %, and it increases up to 90 % after 10 hours by using IO films. For porous and dense films, the degradation varies, respectively, from 29 and 24 % after 2 h, up to 67 and 60 % after 10 hours. The smallest degradation, less than 40 % for 10 h, was obtained by using the rutile single-crystal as photocatalyst.
The variation over the time of the degradation percentage of MB is shown in logarithmic scale in Figure 7.b. It displays a linear variation for the IO films in the whole time range studied for this sample, which corresponds to a first order kinetic

	Apparent reaction rate constant, k (h^{-1})	
Photocatalyst	$t < 8$ h	$t > 8$ h
TiO_2 rutile crystal	$k_1 = 0.084$ (± 0.005)	$k_2 = 0.024$ (± 0.008)
Dense TiO_2 film	$k_1 = 0.127$ (± 0.005)	$k_2 = 0.034$ (± 0.008)
Porous TiO_2 film	$k_1 = 0.172$ (± 0.005)	$k_2 = 0.089$ (± 0.008)
TiO_2 Inverse opals	$k = 0.249$ (± 0.005)	

Table 2
Apparent reaction rate constant of the degradation of a 1 μmol/L MB solution in the presence of different TiO_2 catalyst under UV irradiation.

law given by equation 2:

$$\ln(C_0/C_t) = k \cdot t \tag{2}$$

where k is the apparent reaction rate constant. This is in agreement with the hypothesis assuming that the degradation reaction is an unimolecular elementary reaction. Consequently, the reaction rate is proportional to the concentration of the reactant [38,39].

For the other catalysts, we observed a linear variation for times up to about 8 hours, followed by a decrease of the slope leading to a slower linear variation. Attempts to adjust the experimental data to the expressions corresponding to different-order reactions did not lead to satisfying results. The values of the apparent reaction constant obtained for each catalyst are given in Table 2. A single value of the apparent reaction constant, k, is given in case of IO films. For the other catalysts, two values, k_1 and k_2, are given for $t < 8h$ and $t > 8h$, respectively.

In order to explain the slowing down of degradation kinetics, the effect of the adsorption of the degradation products on the catalyst surface has been addressed. The degradation of MB in presence of TiO_2 is a heterogeneous catalysis process, in particular a contact catalysis process. The reaction takes place in three main steps: the adsorption of the MB molecules on the catalyst surface, the degradation of the adsorbed molecules, and the desorption of the reaction products [38,39]. In a steady state approach, assuming that the adsorption is nearly equilibrated (quasi-equilibrated), the surface reaction is the rate-determining step. The overall reaction rate can be written as follows (eq. 3):

$$k = k_s \cdot \frac{K_{MB} \cdot C_{MB}}{1 + K_{MB} \cdot C_{MB}} \tag{3}$$

with k the reaction rate, k_s the rate constant, K_{MB} the equilibrium constant for the absorption of methylene blue molecules and C_{MB} the concentration of methylene blue. The degradation of MB molecules leads to the apparition of many products

that can be adsorbed on the TiO_2 surface on the same active sites as MB [40]. If the degradation products can also be adsorbed to the catalyst surface, the overall reaction rate can be written as follows (eq. 4) [38,39]:

$$k = k_s \cdot \frac{K_{MB} \cdot C_{MB}}{1 + K_{MB} \cdot C_{MB} + K_P \cdot C_P} \tag{4}$$

with K_P the equilibrium constant for the absorption of reaction products and C_P the concentration of reaction products.
Initially, the concentration of products in the solution can be neglected compared to the concentration of the reactant. The product $K_{MB}.C_{MB}$ exceeds $K_P.C_P$, and the reaction rate is proportional to the apparent rate constant, k_s.
In the case of IO films, the specific surface is higher compared to the other catalysts. This explains the higher value of the apparent rate constant (Table 2). Porous and dense films show a similar behavior, so the specific surface would be similar.
For long times, when the adsorption of the degradation products is in competition with that of the reactants, the overall reaction rate is reduced. For the IO films, we do not observe this effect which is in agreement with high surface available for the adsorption of MB molecules. For the other catalysts, this effect can explain the slowing-down of the reaction kinetics observed for long times. When $K_P.C_P$ is by far the predominant term in the denominator of eq. 4, the reaction rate can be approximated by eq. 5:

$$k = k_s \cdot \frac{K_{MB} \cdot C_{MB}}{K_P \cdot C_P} \tag{5}$$

The increase of C_P in the solution induces the reduction of the reaction rate. One can expect that porous films display more sites available for adsorption than the dense films, which reduces C_P and leads to a smaller slowing-down effect compared to dense films.

4 Conclusions

Inverse opals (IO) films of TiO_2 have been synthesized by ALD using as a template ordered layers of polystyrene beads deposited on a Si substrate by spin coating. Stoichiometric TiO_2 was crystallized in the anatase phase after annealing of the films.
The photocatalytic properties of IO films for the degradation under UV irradiation of methylene blue (MB) in water solutions and the photodegradation kinetics have been investigated. For this, the optical absorption spectrum of MB has been measured as a function of the UV irradiation time. The results have been compared to those obtained for dense and porous planar TiO_2 films deposited on silicon sub-

strates by using the same ALD conditions used for the synthesis of IO films, and a rutile single-crystal catalyst.

It has been shown that the fastest photodegradation of MB is obtained by using IO films as photocatalyst, while the slowest one is obtained with a rutile single-crystal. Porous planar films lead to a degradation kinetics slightly faster than dense films. These results are in agreement with the expected difference in the specific surface of the catalysts as a function of the morphology and the compactness of the films.

After 2 h of UV irradiation, the degradation of MB was about 42 % for IO films, whereas it was about 29 % for porous planar films, 24 % for dense planar films, and only 18 % for rutile single-crystal. The photo-degradation of MB reached 90 % after 10 h by using IO films as a catalyst, which is 35 % more than that obtained with porous planar films. Lower MB degradation percentages, 60 and 40 %, have been obtained with dense TiO_2 films and the rutile single-crystal, respectively.

For the IO films, it has been shown that the degradation kinetics fits a first-order law up to 10 h of UV irradiation. For the other catalysts, the degradation kinetics fits a first-order law up to about 8 hours. The apparent reaction rate constant in this range is slightly higher for porous planar films compared to dense films. Above 10 h, the degradation kinetics is slowed-down, mainly for the dense TiO_2 planar film and the rutile single-crystal. The adsorption of the degradation products at the catalyst surface has been addressed to explain this effect.
The results highlight the potential of IO TiO_2 films synthesized by ALD for photocatalytic applications.

Acknowledgements

The authors acknowledge F. Herbst and O. Heintz from the ICB laboratory for their help in SEM observations and XPS analysis, respectively.

Appendix A. Supplementary data

Supplementary data associated with this article can be found in the online version.

References

[1] O. Carp, C. Huisman, A. Reller, Photoinduced reactivity of titanium dioxide, Progress in Solid State Chemistry 32 (1) (2004) 33 – 177.

[2] L. Armelao, D. Barreca, G. Bottaro, A. Gasparotto, C. Maccato, C. Maragno, E. Tondello, U. L. Štangar, M. Bergant, D. Mahne, Photocatalytic and antibacterial activity of TiO_2 and Au/TiO_2 nanosystems, Nanotechnology 18 (2007) 375709.

[3] C. G. Silva, R. Juárez, T. Marino, R. Molinari, H. García, Influence of excitation wavelength (UV or visible light) on the photocatalytic activity of titania containing gold nanoparticles for the generation of hydrogen or oxygen from water, Journal of the American Chemical Society 133 (3) (2011) 595 – 602.

[4] K. Nakata, T. Ochiai, T. Murakami, A. Fujishima, Photoenergy conversion with TiO_2 photocatalysis: New materials and recent applications, Electrochimica Acta 84 (2012) 103 – 111.

[5] J. Löckinger, S. Nishiwaki, T. P. Weiss, B. Bissig, Y. E. Romanyuk, S. Buecheler, A. N. Tiwari, TiO_2 as intermediate buffer layer in $Cu(In,Ga)Se_2$ solar cells, Solar Energy Materials and Solar Cells 174 (2018) 397 – 404.

[6] K. Nakata, A. Fujishima, TiO_2 photocatalysis: Design and applications, Journal of Photochemistry and Photobiology C: Photochemistry Reviews 13 (3) (2012) 169 – 189.

[7] F. Orts, A. I. del Río, J. Molina, J. Bonastre, F. Cases, Study of the reuse of industrial wastewater after electrochemical treatment of textile effluents without external addition of chloride, International Journal of Electrochemical Science (2019) 1733 – 1750.

[8] L. Mouni, L. Belkhiri, J.-C. Bollinger, A. Bouzaza, A. Assadi, A. Tirri, F. Dahmoune, K. Madani, H. Remini, Removal of methylene blue from aqueous solutions by adsorption on kaolin: Kinetic and equilibrium studies, Applied Clay Science 153 (2018) 38 – 45.

[9] N. Serpone, A. V. Emeline, Semiconductor photocatalysis — past, present, and future outlook, The Journal of Physical Chemistry Letters 3 (2012) 673 – 677.

[10] Y.-R. Liu, Y.-C. Hsueh, T.-P. Perng, Fabrication of TiN inverse opal structure and Pt nanoparticles by atomic layer deposition for proton exchange membrane fuel cell, International Journal of Hydrogen Energy 42 (15) (2017) 10175 – 10183.

[11] X. Li, M. Puttaswamy, Z. Wang, C. K. Tan, A. C. Grimsdale, N. P. Kherani, A. I. Y. Tok, A pressure tuned stop-flow atomic layer deposition process for MoS_2 on high porous nanostructure and fabrication of TiO_2/MoS_2 core/shell inverse opal structure, Applied Surface Science 422 (2017) 536 – 543.

[12] V. O. Williams, E. J. DeMarco, M. J. Katz, J. A. Libera, S. C. Riha, D. W. Kim, J. R. Avila, A. B. F. Martinson, J. W. Elam, M. J. Pellin, O. K. Farha, J. T. Hupp, Fabrication of transparent-conducting-oxide-coated inverse opals as mesostructured architectures for electrocatalysis applications: A case study with NiO, ACS Applied Materials & Interfaces 6 (2014) 12290 – 12294.

[13] K.-Y. Yoon, J.-S. Lee, K. Kim, C. H. Bak, S.-I. Kim, J.-B. Kim, J.-H. Jang, Hematite-based photoelectrochemical water splitting supported by inverse opal structures of graphene, ACS Applied Materials & Interfaces 6 (2014) 22634 – 22639.

[14] K. P. Furlan, R. M. Pasquarelli, T. Krekeler, M. Ritter, R. Zierold, K. Nielsch, G. A. Schneider, R. Janssen, Highly porous α-Al_2O_3 ceramics obtained by sintering atomic layer deposited inverse opals, Ceramics International 43 (14) (2017) 11260 – 11264.

[15] G. I. Waterhouse, M. R. Waterland, Opal and inverse opal photonic crystals: Fabrication and characterization, Polyhedron 26 (2007) 356 – 368.

[16] J. I. L. Chen, G. von Freymann, S. Y. Choi, V. Kitaev, G. A. Ozin, Amplified photochemistry with slow photons, Advanced Materials 18 (2006) 1915 – 1919.

[17] Y. Li, F. Piret, T. Léonard, B.-L. Su, Rutile TiO_2 inverse opal with photonic bandgap in the UV–visible range, Journal of Colloid and Interface Science 348 (2010) 43 – 48.

[18] J. Yu, J. Lei, L. Wang, J. Zhang, Y. Liu, TiO_2 inverse opal photonic crystals: Synthesis, modification, and applications - a review, Journal of Alloys and Compounds 769 (2018) 740 – 757.

[19] S. Zhuiykov, M. Akbari, Z. Hai, C. Xue, H. Xu, L. Hyde, Data set for fabrication of conformal two-dimensional TiO_2 by atomic layer deposition using tetrakis (dimethylamino) titanium (TDMAT) and H_2O precursors, Data in Brief 13 (2017) 401 – 407.

[20] P. Violet, E. Blanquet, D. Monnier, I. Nuta, C. Chatillon, Experimental thermodynamics for the evaluation of ALD growth processes, Surface and Coatings Technology 204 (6) (2009) 882 – 886.

[21] P. Borylo, K. Lukaszkowicz, M. Szindler, J. Kubacki, K. Balin, M. Basiaga, J. Szewczenko, Structure and properties of Al_2O_3 thin films deposited by ALD process, Vacuum 131 (2016) 319 – 326.

[22] A. Purniawana, P. Frencha, G. Pandraudb, P. Sarrob, TiO_2 ALD nanolayer as evanescent waveguide for biomedical sensor applications, Procedia Engineering 5 (2010) 1131 – 1135.

[23] D. J. H. Emslie, P. Chadha, J. S. Price, Metal ALD and pulsed CVD: Fundamental reactions and links with solution chemistry, Coordination Chemistry Reviews 257 (23) (2013) 3282 – 3296.

[24] M. Sarr, N. Bahlawane, D. Arl, M. Dossot, E. McRae, D. Lenoble, Atomic layer deposition of cobalt carbide films and their magnetic properties using propanol as a reducing agent, Applied Surface Science 379 (2016) 523 – 529.

[25] M. Lai, J. Zhao, Q. Chen, S. Feng, Y. Bai, Y. Li, C. Wang, Photocatalytic toluene degradation over Bi-decorated TiO_2: Promoted O_2 supply to catalyst's surface by metallic Bi, Catalysis Today 335 (2019) 372 – 380.

[26] L. Avril, S. Bourgeois, M. C. Marco de Lucas, B. Domenichini, P. Simon, F. Addou, J. Boudon, V. Potin, L. Imhoff, Thermal stability of Au/ TiO_2 nanocomposite films prepared by direct liquid injection CVD, Vacuum 122 (2015) 314 – 320.

[27] L. Avril, S. Reymond-Laruinaz, J. Decams, S. Bruyère, V. Potin, M. C. Marco de Lucas, L. Imhoff, TiO_2 anatase films obtained by direct liquid injection atomic layer deposition at low temperature, Applied Surface Science 288 (2014) 201 – 207.

[28] I. J. Raaijmakers, Low temperature metal-organic chemical vapor deposition of advanced barrier layers for the microelectronics industry, Thin Solid Films 247 (1994) 85 – 93.

[29] Y. J. Kim, D. Lim, H. H. Han, A. S. Sergeevich, Y.-R. Jeon, J. H. Lee, S. K. Son, C. Choi, The effects of process temperature on the work function modulation of ALD HfO_2 MOS device with plasma enhanced ALD TiN metal gate using TDMAT precursor, Microelectronic Engineering 178 (2017) 284 – 288.

[30] B. Abendroth, T. Moebus, S. Rentrop, R. Strohmeyer, M. Vinnichenko, T. Weling, H. Stöcker, D. C. Meyer, Atomic layer deposition of TiO_2 from tetrakis(dimethylamino)titanium and H_2O, Thin Solid Films 545 (2013) 176 – 182.

[31] S. Boukrouh, R. Bensaha, S. Bourgeois, E. Finot, M. C. Marco de Lucas, Reactive direct current magnetron sputtered TiO_2 thin films with amorphous to crystalline structures, Thin Solid Films 516 (2008) 6353 – 63587.

[32] C. Ferrari, J. Robertson, Raman spectroscopy of amorphous, nanostructured, diamond-like carbon, and nanodiamond, Phil. Trans. R. Soc. Lond. A 362 (2004) 2477 – 2512.

[33] A. R. Burke, C. R. Brown, W. C. Bowling, J. E. Glaub, D. Kapsch, C. M. Love, R. B. Whitaker, W. E. Moddeman, Ignition mechanism of the titanium–boron pyrotechnic mixture, Surface and Interface Analysis 11 (1988) 353 – 358.

[34] F. Werfel, O. Brümmer, Corundum structure oxides studied by XPS, Physica Scripta 28 (1983) 92 – 96.

[35] M. Takagi-Kawai, M. Soma, T. Onishi, K. Tamaru, The adsorption and the reaction of NH_3 and NO_x on supported V_2O_5 catalysts: Effect of supporting materials, Canadian Journal of Chemistry 58 (2011) 2132 – 2137.

[36] L. Setiawan, H. Baumann, D. Gribbin, Surface studies of keratin fibres and related model compounds using ESCA. I - Intermediate oxidation products of the model compound l-cystine and their hydrolytical behaviour, Surface and Interface Analysis 7 (1985) 188 – 195.

[37] N. Florence, H. Naorem, Dimerization of methylene blue in aqueous and mixed aqueous organic solvent: A spectroscopic study, Journal of Molecular Liquids 198 (2014) 255 – 258.

[38] M. Prettre, B. Claudel, Elements of Chemical Kinetics, Gordon and Breach Science Publishers, 1970.

[39] M. E. Davis, R. J. Davis, Fundamentals of Chemical Reaction Engineering, McGraw-Hill, New York, 2003.

[40] A. Houas, H. Lachheb, M. Ksibi, E. Elaloui, C. Guillard, J.-M. Herrmann, Photocatalytic degradation pathway of methylene blue in water, Applied Catalysis B: Environmental 31 (2001) 145 – 157.